Research Article

Spectrum of the Anomalous Microwave Emission in the North Celestial Pole with *WMAP* 7-Year Data

Anna Bonaldi[1] and Sara Ricciardi[2]

[1] *Jodrell Bank Centre for Astrophysics, School of Physics and Astronomy, the University of Manchester,*
  Alan Turing Building, Oxford Road, Manchester M13 9PL, UK
[2] *INAF-IASF Bologna, Via Gobetti 101, Bologna, Italy*

Correspondence should be addressed to Anna Bonaldi, anna.bonaldi@manchester.ac.uk

We estimate the frequency spectrum of the diffuse anomalous microwave emission (AME) on the North Celestial Pole (NCP) region of the sky with the Correlated Component Analysis (CCA) component separation method applied to *WMAP* 7-yr data. The NCP is a suitable region for this analysis because the AME is weakly contaminated by synchrotron and free-free emission. By modeling the AME component as a peaked spectrum we estimate the peak frequency to be 21.7 ± 0.8 GHz, in agreement with previous analyses which favored $\nu_p < 23$ GHz. The ability of our method to correctly recover the position of the peak is verified through simulations. We compare the estimated AME spectrum with theoretical spinning dust models to constrain the hydrogen density n_H. The best results are obtained with densities around 0.2–0.3 cm^{-3}, typical of warm ionised medium (WIM) to warm neutral medium (WNM) conditions. The degeneracy with the gas temperature prevents an accurate determination of n_H, especially for low hydrogen ionization fractions, where densities of a few cm^{-3} are also allowed.

1. Introduction

The anomalous microwave emission (AME) component is highly correlated with the far infrared dust emission [1–10] and is believed to be the electric dipole radiation from small spinning dust grains [11]. Spinning dust models predict a peaked spectrum ranging 10–150 GHz depending on the local physical conditions [12, 13]. Probing the peak of the emission enables us to compare models with observations and is the best way to distinguish the AME from synchrotron emission and free-free emission, both having a power-law spectrum.

The AME has been studied in individual dust clouds associated with reflection nebulae, molecular clouds, photo-dissociation regions, and HII regions [14, 15]. The best examples of peaked AME spectra are probably the Perseus and ρ Ophiuchi molecular clouds, which have been probed with high accuracy thanks to the availability of many different datasets. In these regions the derived peak is at ~30 GHz [14].

The study of the AME in more diffuse regions essentially becomes a component separation problem, which is often complicated by the lack of low-frequency data covering large sky areas. Diffuse dust-correlated emission has been detected with COBE-DMR [2] and *WMAP* data [4, 7, 16–18]; however the details of the spectrum are still unclear. Template-fitting analyses show that the dust-correlated emission between 20 and 60 GHz is well described by a power-law [2, 4, 7, 18]. Given the error bars, a peaked spectrum is not ruled out, but a low peak frequency (<23 GHz) is favored. Alternatively, the observed spectrum could result from the superposition of multiple peaked components. The component separation analysis done by [17] found that a peaked AME model gives better results in terms of CMB cleaning, however no estimation of the AME peak frequency was attempted.

In this work we address the estimation of the peak frequency of the diffuse AME on *WMAP* 7-yr data complemented by ancillary data with the Correlated Component Analysis (CCA, [19]) component separation method. We

consider the North Celestial Pole (NCP) region of the sky, centered on Galactic coordinates $(l, b) \sim (125°, 25°)$. As already noted by [4], this region of the sky is particularly suited for this analysis since there is significant thermal and anomalous dust emission, while synchrotron emission and free-free emission (traced by the 408 MHz from [20] and the Hα map from [21]) are faint.

2. Description of the Method

In the following we describe the principles of operation of the harmonic-domain CCA; for further details we refer the reader to [19]. The CCA [19, 22] exploits second-order statistics to estimate the frequency scaling of the components from the statistics of data and noise. For each position on the sky (each pixel) we write our data model as

$$\mathbf{x}(r) = [\mathbf{B} * \mathbf{Hs}](r) + \mathbf{n}(r), \qquad (1)$$

where $\mathbf{s}$ is a vector whose elements contain the different components (CMB, free-free emission, synchrotron emission, thermal dust emission, AME); $\mathbf{x}$ and $\mathbf{n}$ are vectors too, each element containing, respectively, the data and the instrumental noise for each frequency. The diagonal matrix $\mathbf{B}$ contains the instrumental beams for all frequency channels and $*$ denotes convolution. The matrix $\mathbf{H}$ is called the mixing matrix and it contains the frequency scaling of the components for all the considered frequencies.

By translating (1) in the harmonic domain, the convolution becomes a multiplication and the data model becomes a linear mixture. For each transformed mode (ℓ) we can write

$$\mathbf{X}(\ell) = \widetilde{\mathbf{B}}(\ell)\mathbf{HS}(\ell) + \mathbf{N}(\ell), \qquad (2)$$

where $\mathbf{X}$, $\mathbf{S}$, and $\mathbf{N}$ are the transforms of $\mathbf{x}$, $\mathbf{s}$, and $\mathbf{n}$, respectively, and $\widetilde{\mathbf{B}}$ is the transform of the matrix $\mathbf{B}$. The cross-spectra of the data $\widetilde{\mathbf{C}}_{\mathbf{x}}(\ell)$, sources $\widetilde{\mathbf{C}}_{\mathbf{s}}(\ell)$ and noise, $\widetilde{\mathbf{C}}_{\mathbf{n}}(\ell)$, are related by

$$\widetilde{\mathbf{C}}_{\mathbf{x}}(\ell) - \widetilde{\mathbf{C}}_{\mathbf{n}}(\ell) = \widetilde{\mathbf{B}}(\ell)\mathbf{H}\widetilde{\mathbf{C}}_{\mathbf{s}}(\ell)\mathbf{H}^T\widetilde{\mathbf{B}}^{\dagger}(\ell), \qquad (3)$$

where the dagger superscript denotes the adjoint matrix.

The left-hand side of (3) can be estimated from the data for a suitable set of spectral bins $\widehat{\ell}$; this is used by CCA to estimate the mixing matrix and the source cross-spectra on the right-hand side of the equation. Due to the scaling ambiguity of the problem, the mixing matrix is normalized at a reference frequency. To reduce the number of unknowns, the mixing matrix is parametrized through a parameter vector $\mathbf{p}$ (such that $\mathbf{H} = \mathbf{H}(\mathbf{p})$), by adopting suitable fitting relations for the spectra of the astrophysical components (as detailed in the next section).

By using two-dimensional discrete Fourier transforms it is possible to apply the harmonic-domain CCA to square sky patches. This approach is advisable as the mixing matrix varies on the sky. The HEALPix ([24]) data on the sphere are projected on the plane tangential to the center of the patch and re-gridded with a suitable number of bins in order to correctly sample the original resolution. The patch

size is obtained as a trade-off between the need of having uniform spectral properties of the foregrounds and enough statistics for a robust computation of the auto- and cross-spectra of the data. In the present analysis we use a patch size of 30° × 30°. By using higher resolution data (e.g., *Planck* data) it is possible to reduce the patch size by carrying the analysis up to a larger multipole. We analyzed the sky patch centered on $(l, b) = (124°, 26°)$ (shown in Figure 1) and verified the stability of the results for a sample of patches shifted in latitude and longitude up to 10°.

3. Description of the Analysis

We used the following datasets:

(i) *WMAP* 7-yr K, Ka, Q, V, and W bands [25]. All maps have been used at the original resolution except the K band, which has been smoothed to 1° resolution to reduce the effect of beam asymmetry;

(ii) 408 MHz map [20] to trace the synchrotron component;

(iii) predicted free-free emission at 23 GHz based on the Hα map by [21] corrected for dust absorption with the E(B-V) map by [26] assuming $f_d = 0.3$;

(iv) predicted dust emission at 94 GHz by [23].

The different resolution of the data maps is accounted for with the beam matrix $\widetilde{\mathbf{B}}$ in (3). In particular, the beams are deconvolved for the mixing matrix estimation. The noise properties for the *WMAP* maps have been computed by simulating different noise realizations starting from the input N_{obs} maps and σ_0 values. For the maps used as foreground templates (408 MHz map, 23 GHz free-free map, and 94 GHz dust prediction) we assumed a Gaussian noise at the 10% level, which is much higher than the instrumental noise. This extra noise mimics the error on the template as a tracer of the true component, the 10% level being indicative. We verified, however, that the results are not sensitive to the exact value assumed. We modeled the data as a mixture of five components: CMB, synchrotron emission, thermal dust emission, free-free emission, and AME. Each frequency map contributes five elements to the mixing matrix, one for each component. The synchrotron, free-free and dust templates are used as frequency channels having only one mixing matrix entry, that of the corresponding component, different from zero.

It is worth noting that, compared with previous work, we are not assuming correlation between the AME and thermal dust emission and we are not exploiting any template for the AME. Though the AME and the thermal dust emission are significantly correlated, the correlation is not supposed to be perfect, as, according to spinning dust models, the AME traces the distribution of smaller dust grains (PAHs). Indeed, the intensity ratio of AME and thermal dust is found to vary in the sky by a factor of ~2 (e.g., [4]).

We estimated the frequency spectrum of the AME while assuming the spectra of the other components to be known. For CMB we used the usual black-body law with temperature
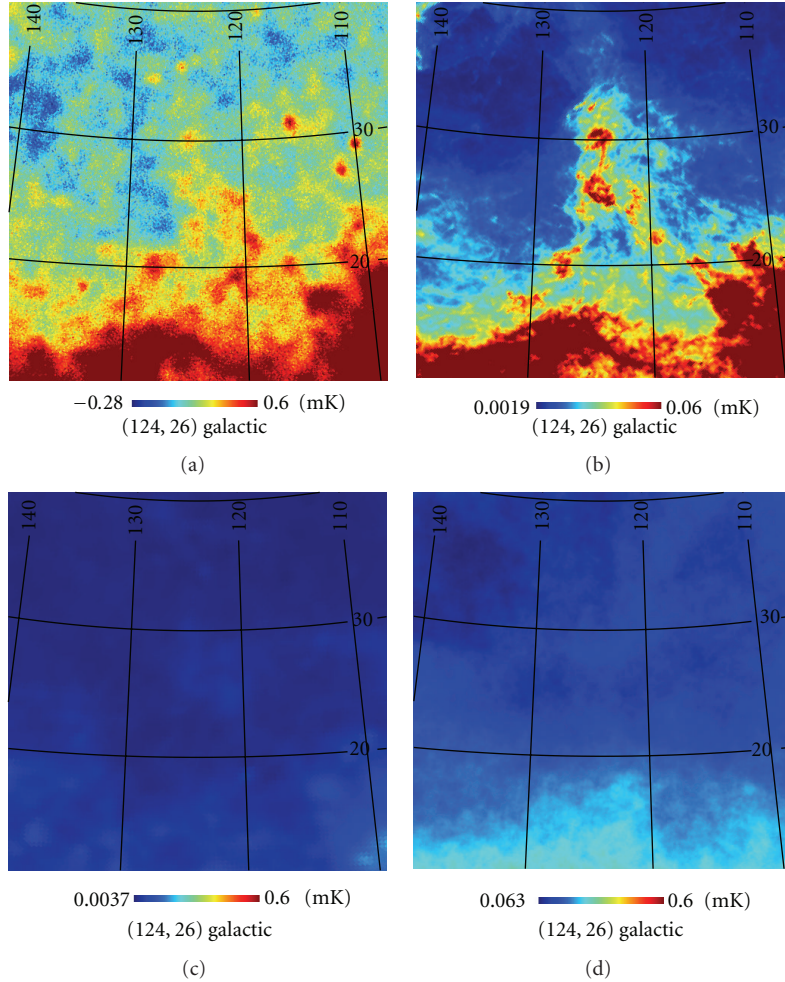
FIGURE 1: Maps of the region of interest. *WMAP* K band (a), 94 GHz dust prediction (b, [23]). free-free (c) and synchrotron (d) predictions at 23 GHz based on the Hα map ([21]) and the 408 MHz map ([20]) assuming a spectral index $\beta_s = -2.9$.

of 2.726 K ([27]); for free-free we used the model $T_{\mathrm{RJ,ff}}(\nu) \propto G \times (\nu/10)^{-2}$ where $G = 3.96\,(T_4)^{0.21}(\nu/40)^{-0.14}$ is the Gaunt factor, which is responsible for the departure from a pure power-law behavior, and $T_4 = 0.7$ is the electron temperature T_e in units of 10^4 K. The thermal dust emission has been modeled as a grey-body with temperature $T_d = 18$ K and spectral index $\beta_d = 1.7$. This is consistent with the 1-component dust model by [23]; *Planck* data, extending the observations up to 857 GHz, will allow a refinement of this model. For synchrotron we assumed a power-law scaling with spectral index $\beta_s = -2.9$.

For the AME we used the parametric relation proposed by [17]

$$\log T_{\mathrm{RJ,ame}}(\nu) \propto \left(\frac{m_{60}\log \nu_p}{\log\left(\nu_p/60\right)} + 2 \right) \log \nu + \frac{m_{60}\left(\log \nu\right)^2}{2\log\left(\nu_p/60\right)},$$

(4)

which is a parabola in the $\log(\nu) - \log(S)$ plane parametrized in terms of peak frequency ν_p and slope at 60 GHz m_{60}. The CCA solves for the two parameters m_{60} and ν_p, so the accuracy of the estimation of the AME peak frequency ν_p is

related to the ability of the parametric relation to reproduce the true spectrum. We verified, however, that this parametric model can fit a wide range of spinning dust spectra. This is shown in **Figure 2**, comparing spinning dust spectra produced with the SpDust [12, 28] code with the results of the fit of (4) obtained by minimizing the χ^2 for the set of frequencies considered in this work. The physical models that we consider are: warm neutral medium (WNM), cold neutral medium (CNM), warm ionised medium (WIM), and molecular cloud (MC). In general, the fits are accurate up to 61 GHz, while at 94 GHz the parametric relation may not be able to reproduce the input spectra in detail. This is a consequence of fitting complex spectra with only a few parameters, the fit being less accurate where the AME is weaker. The best-fit parameters that we obtain, reported in Table 1, vary significantly from one input model to another.

4. Test on Simulated Data

We simulated *WMAP* 7-yr data by assuming monochromatic band-passes centered at the central frequency of the realistic

TABLE 1: Parameters for the spectra in Figure 2. The SpDust input parameters are as follows: the total hydrogen number density n_H, the gas temperature T, the intensity of the radiation field relative to the average interstellar radiation field χ, the hydrogen ionization fraction $x_H = n_{H^+}/n_H$, and the ionized carbon fractional abundance $x_C = n_{C^+}/n_H$. We also report the CCA spectral parameters ν_p, m_{60} (4).

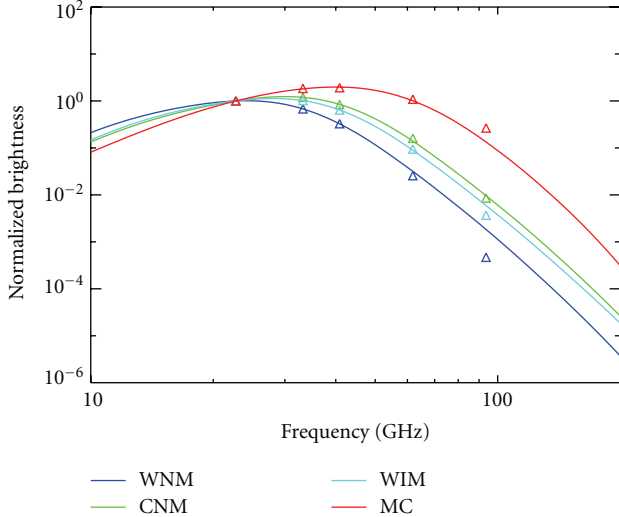| Model name	n_H [cm^{-3}]	T [K]	χ	x_H	x_C	ν_p	m_{60}
WNM	0.4	6000	1.00	0.10	0.0003	24.34	7.64
CNM	30.0	100	1.00	0.0012	0.0003	29.26	5.31
WIM	0.1	8000	1.00	0.99	0.001	27.64	5.99
MC	300	20	0.01	0.0	0.0001	38.13	2.23

FIGURE 2: Theoretical spinning dust models produced with SpDust (solid lines) and fitted with CCA parametric model (triangles, same color of the model). Input SpDust parameters and best-fit parameters for the CCA model are provided in Table 1.

bands, Gaussian beams at the nominal values, Gaussian noise generated according to realistic (spatially varying) RMS. Our model of the sky consists of the following components:

   (i) CMB emission constrained by the best-fit power spectrum model to *WMAP* 7-yr;

   (ii) synchrotron emission given by [20] scaled in frequency with a power-law model with a spatially varying synchrotron spectral index β_s as modeled by [29];

   (iii) free-free component modeled by the Hα map of [21] corrected for dust absorption with the E(B-V) map from [26] with $f_d = 0.3$ and scaled in frequency with a power-law with fixed spectral index of -2.14;

   (iv) thermal dust emission modeled with the 100 μm map from [26] scaled in frequency with the best-fit model by [23] which consists of two grey-body laws having different temperatures and emissivity indices;

   (v) AME emission modeled by the E(B-V) map from [26] with intensity at 23 GHz calibrated on the results by [4] for average intermediate-latitude conditions and scaled according to SpDust models.

It is worth noting that this sky model is more complex than the spectral model assumed in the component separation. The synchrotron spectral index is spatially varying and both the thermal dust AME spectra, though spatially constant, are not generated with the CCA parametric models. This has been done purposely, to reflect a more realistic situation. To test the ability of our pipeline to recover the AME spectrum in different situations, we adopted two SpDust models for the AME: one peaking at 26 GHz and the other peaking at 19 GHz.

We performed an estimate of the AME spectrum on the simulated data following the same procedure applied to the real data. The results are presented in Figure 3. For AME peaking at 26 GHz the recovery of the spectrum is very accurate; the result on the peak frequency is $\nu_p = 26.5 \pm 0.5$. The accuracy of the estimation is helped by the weak synchrotron and free-free contamination in this region of the sky (in a more general case the error on ν_p would be of a few GHz). With the AME peaking at 19 GHz the errors increase, but the recovery of the spectrum is still satisfactory; we obtain $\nu_p = 18.5 \pm 1.5$. Our pipeline is able to distinguish very clearly between the two input models and to correctly estimate the peak frequency of the AME in both cases.

5. Results

The results for the AME spectrum on the NCP are shown in Figure 4; the estimated peak frequency is $\nu_p = 21.7 \pm 0.8$. The diamonds with error bars are the AME mixing matrix elements at *WMAP* frequencies and related uncertainties derived from the results on ν_p and m_{60}.

By comparing these data points with theoretical models produced with SpDust we can constrain the physical properties of the medium with the hypothesis of spinning dust emission. Some relevant parameters of the SpDust code are: hydrogen number density n_H (cm^{-3}); gas temperature T (K); intensity of the radiation field with respect to average Galactic conditions, χ, and hydrogen ionization fraction, x_H. Advanced parameters describe the dust grains and define the abundance of other elements.

The hydrogen density n_H is sensitive to the position of the peak and in general to the shape of the spectrum in the considered frequency range. It is also degenerate with other parameters, in particular the gas temperature T. We investigated this degeneracy by sampling the 2-dimensional n_H-T space with a grid approach while conditioning the remaining parameters. For each point in the parameter space we computed the likelihood as $\Lambda = \exp(-\chi^2/2)$ where χ^2
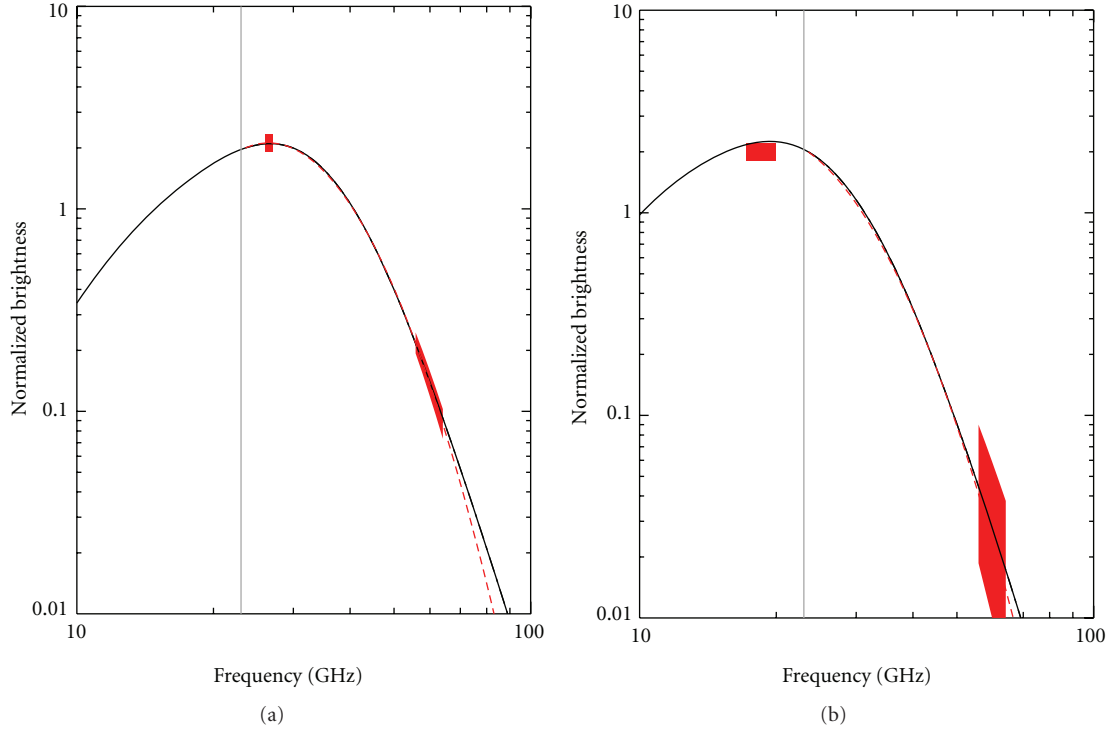
(a)

(b)

FIGURE 3: Comparison of true input AME spectra (black solid lines) with CCA estimates (red dashed lines) for two AME models, one peaking at 26 GHz (a) and one at 19 GHz (b). The red shaded areas show the recovered ν_p and m_{60} with 1σ error bar. The results for the peak frequency are $\nu_p = 26.5 \pm 0.5$ and $\nu_p = 18.5 \pm 1.5$ for (a) and (b), respectively. The grey vertical lines indicate the frequency of 23 GHz which sets the limit of our data.
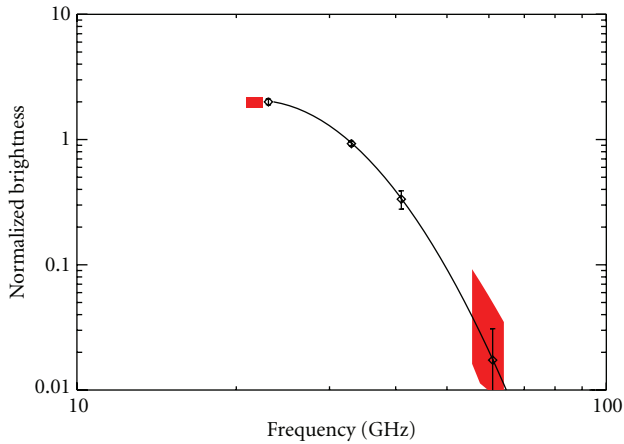

FIGURE 4: Best-fit AME model (black line) and results in terms of ν_p and m_{60} considering 1σ uncertainties (red areas). The peak frequency results $\nu_p = 21.7 \pm 0.8$. Diamonds with error bars are the results in terms of normalized intensity at *WMAP* bands and related uncertainties.

TABLE 2: Statistics for n_H marginalized over T corresponding to the results of Figure 5.

x_H	χ	n_H	Δn_H^-	Δn_H^+
0.001	1	0.3	0.1	0.9
0.01	1	0.3	0.1	0.7
0.1	1	0.25	0.09	0.07
0.001	0.1	0.4	0.1	1.2

is the standard chi-square. In computing the χ^2 we did not consider the 94 GHz data point, which could be biased, as verified through simulations (see Section 4). We repeated the likelihood estimation for different choices of the parameters x_H and χ (varying all those parameters simultaneously would be computationally too demanding). As the CCA outputs are in normalized units, we compared both the model and the data after scaling each of them by the sum of the intensities at 23, 33, 41 and 61 GHz.

The results of the n_H-T parameter estimation are shown in Figure 5. The colored lines show the likelihoods for n_H for different values of T as detailed in the legend, while the black lines show the likelihood for n_H marginalized over T in the range 100–10000 K. Different panels correspond to different choices for the other parameters: $x_H = 0.001$, $\chi = 1$, on the top left; $x_H = 0.001$, $\chi = 0.1$, on the top right; $x_H = 0.01$, $\chi = 1$, on the bottom left; and $x_H = 0.1$, $\chi = 1$ on the bottom right. The marginalized statistics for n_H are reported in Table 2 (Δn_H^- and Δn_H^+ being the lower and upper 1σ error on n_H). The n_H-T degeneracy weakens the constraint on n_H in particular on the high-density side of the distribution. The degeneracy decreases with increasing hydrogen ionization fraction.
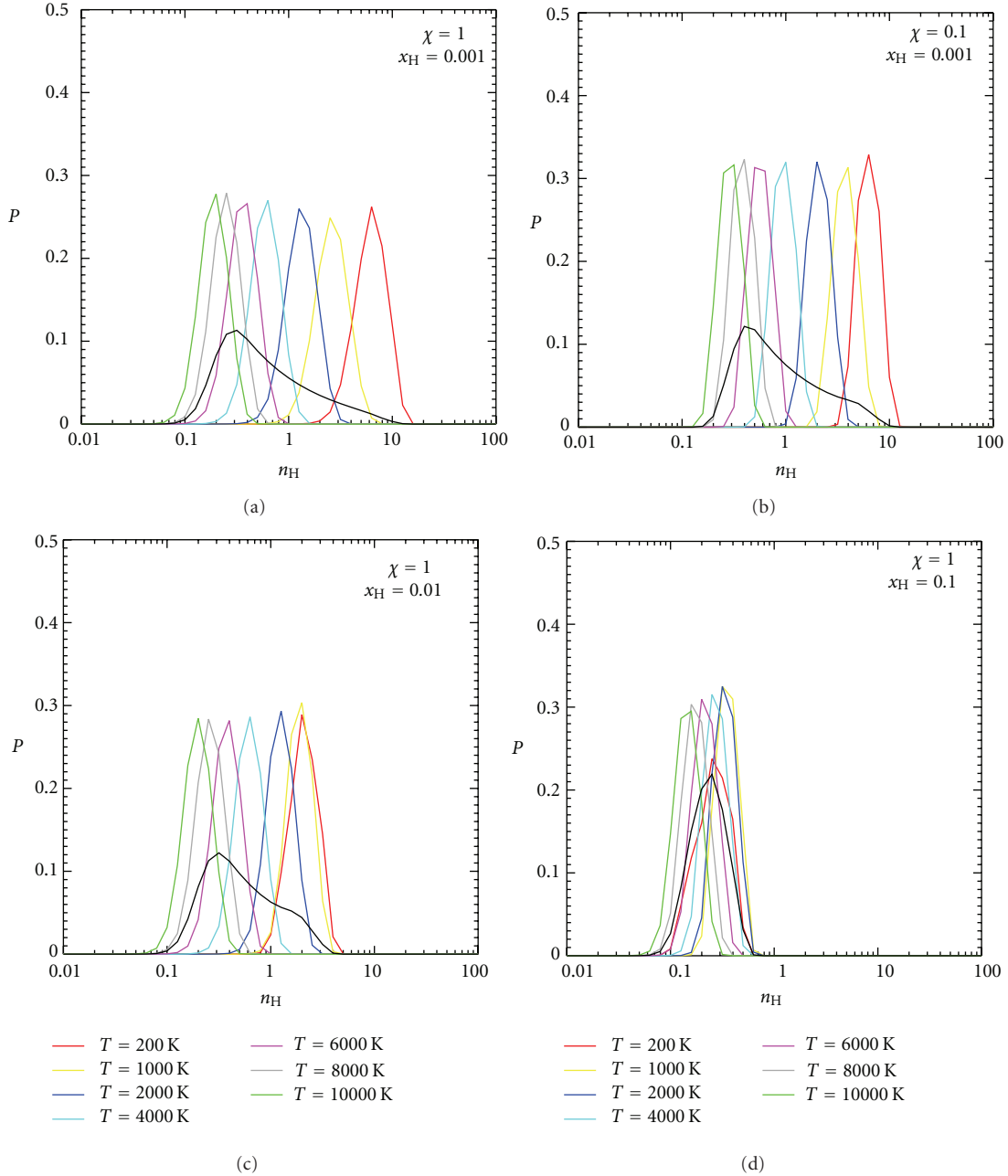
(a)

(b)

(c)

(d)

FIGURE 5: Colored lines: likelihoods for n_H for different values of T as detailed in the legend; black line: likelihood for n_H marginalized over T. (a) $x_H = 0.001$, $\chi = 1$; (b) same as (a) with $\chi = 0.1$; (c, d): same as (a) with $x_H = 0.01$ (c) and $x_H = 0.1$ (d).

The best results are obtained for densities of 0.2–0.4 cm^{-3}, typical of WIM/WNM conditions. In Figure 6 we show the data compared to some SpDust models to exemplify the quality of the fit. The comparison of the red ($n_H = 0.25$ cm^{-3}, $T = 6000$ K, $x_H = 0.1$, $\chi = 1$) and magenta ($n_H = 0.25$ cm^{-3}, $T = 6000$ K, $x_H = 0.01$, $\chi = 1$) lines illustrates the effect of x_H. The blue line corresponds to $n_H = 0.3$ cm^{-3}, $T = 6000$ K, $x_H = 0.31$, $\chi = 1$; compared to the magenta line, it illustrates the effect of increasing n_H. Finally, the cyan ($n_H = 0.40$ cm^{-3}, $T = 6000$ K, $x_H = 0.001$, $\chi = 0.1$) and green ($n_H = 0.40$ cm^{-3}, $T = 6000$ K, $x_H = 0.001$, $\chi = 1$) lines show the effect of χ. The availability of data at frequencies of

a few GHz will be very valuable to improve the constraints on such parameters.

To complement the physical description of the medium we computed the hydrogen column density N_H (cm^{-2}) from the brightness at 100 μm, I_{100}, through I_{100} [MJy sr^{-1}] = $(0.69 \pm 0.03) \times N_H$ [10^{20} cm^{-2}] [30]. We used the IRIS [31] band 4 (100 μm) data and integrated the emission inside a 1° beam centered in $l = 25°$, $b = 125°$, corresponding to bright dust emission (see Figure 1), to compute a representative value for I_{100}. This analysis yields $N_H = (2.9 \pm 0.2) \times 10^{20}$ cm^{-2}, which is a plausible value for the diffuse ISM environment at intermediate latitudes.

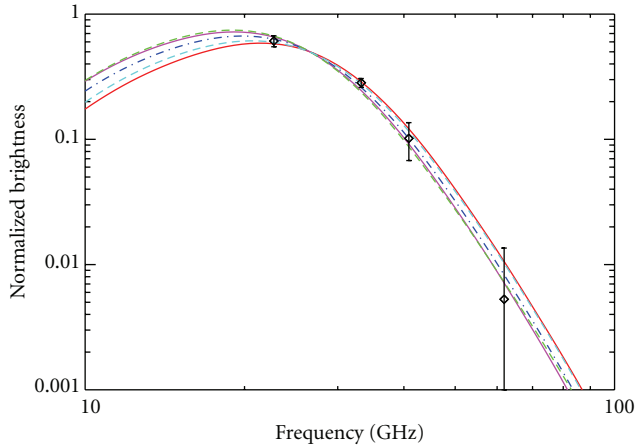FIGURE 6: Comparison between data (diamonds and error bars) and different SpDust models. Red: $n_H = 0.25\,\mathrm{cm}^{-3}$ $T = 6000\,\mathrm{K}$, $x_H = 0.1$, $\chi = 1$; magenta: same as red with $x_H = 0.01$; blue: $n_H = 0.30\,\mathrm{cm}^{-3}$ $T = 6000\,\mathrm{K}$, $x_H = 0.01$, $\chi = 1$; green: $n_H = 0.40\,\mathrm{cm}^{-3}$ $T = 6000\,\mathrm{K}$, $x_H = 0.001$, $\chi = 1$; cyan: same as blue with $\chi = 0.1$.

6. Conclusions

We have studied the spectrum of the diffuse AME with *WMAP* 7-yr and ancillary data in the North Celestial Pole (NCP) region of the sky. In this region the AME dominates the low-frequency emission, as both synchrotron and free-free are faint. Previous template-fitting analysis by [4] found that the AME spectrum in this region is consistent with a power-law above 23 GHz; the same would apply to most diffuse AME at intermediate latitudes [2, 4, 7, 16–18]. This favors a low peak frequency ($\nu_p < 23\,\mathrm{GHz}$).

For our analysis we rely on the CCA component separation method, which exploits the data auto- and cross-spectra to estimate the frequency spectra of the components in terms of a set of spectral parameters. Our method models the AME as a peaked spectrum and fits for the peak frequency, ν_p, and the slope at 60 GHz, m_{60}. We verified with simulations that we are able to correctly recover the AME spectrum and more specifically the peak frequency, even when it is below 23 GHz. We get $\nu_p = 21.7 \pm 0.8\,\mathrm{GHz}$, which is both a confirmation and an improvement of the previous results. This result relies on the assumption that our parametric model for the AME is a good representation of the true spectrum, which has been verified for a wide range of theoretical spinning dust models.

Using the SpDust code, we linked the estimated spectrum to the local physical conditions with the hypothesis of spinning dust emission. We investigated in particular the hydrogen density (n_H [cm^{-3}]), which is sensitive to the position of the peak, and its degeneracy with the gas temperature T [K]. The densities that we get are those typical of WIM/WNM conditions (0.2–0.4 cm^{-3}). For a low hydrogen ionization fraction ($n_H \leq 10^{-2}$), densities up to a few cm^{-3} are allowed by the n_H-T degeneracy. Lower radiation fields (χ) require slightly lower n_H. By considering 100 μm data for our region we obtain a hydrogen column density $N_H \sim 10^{20}\,\mathrm{cm}^{-2}$. Overall, the recovered AME

spectrum is found to be consistent with that predicted by spinning dust models for plausible physical conditions.

Acknowledgments

References

[1] G. Lagache, "The large-scale anomalous microwave emission revisited by WMAP," *Astronomy and Astrophysics*, vol. 405, no. 3, pp. 813–819, 2003.

[2] A. J. Banday, C. Dickinson, R. D. Davies, R. J. Davis, and K. M. Górski, "Reappraising foreground contamination in the COBE-DMR data," *Monthly Notices of the Royal Astronomical Society*, vol. 345, no. 3, pp. 897–911, 2003.

[3] A. Kogut, "Spatial correlation between dust and diffuse ionized gas," in *American Astronomical Society Meeting Abstracts*, vol. 28 of *Bulletin of the American Astronomical Society*, p. 1295, 1996.

[4] R. D. Davies, C. Dickinson, A. J. Banday, T. R. Jaffe, K. M. Górski, and R. J. Davis, "A determination of the spectra of Galactic components observed by the Wilkinson Microwave Anisotropy Probe," *Monthly Notices of the Royal Astronomical Society*, vol. 370, no. 3, pp. 1125–1139, 2006.

[5] N. Ysard, M. A. Miville-Deschênes, and L. Verstraete, "Probing the origin of the microwave anomalous foreground," *Astronomy and Astrophysics*, vol. 509, no. 1, 4 pages, 2010.

[6] B. Gold, N. Odegard, J. L. Weiland et al., "Seven-year wilkinson anisotropy probe (WMAP) observations: galactic foreground emission," *Astrophysical Journal*, vol. 192, no. 2, 2011.

[7] G. Dobler and D. P. Finkbeiner, "Extended anomalous foreground emission in the WMAP three-year data," *Astrophysical Journal Letters*, vol. 680, no. 2, pp. 1222–1234, 2008.

[8] A. De Oliveira-Costa, M. Tegmark, R. D. Davies et al., "The quest for microwave foreground X," *Astrophysical Journal*, vol. 606, no. 2, pp. L89–L92, 2004.

[9] D. P. Finkbeiner, G. I. Langston, and A. H. Minter, "Microwave interstellar medium emission in the green bank galactic plane survey: evidence for spinning dust," *Astrophysical Journal*, vol. 617, no. 1, pp. 350–359, 2004.

[10] E. M. Leitch, A. C. S. Readhead, T. J. Pearson, and S. T. Myers, "An anomalous component of galactic emission," *Astrophysical Journal Letters*, vol. 486, no. 1, pp. L23–L26, 1997.

[11] B. T. Draine and A. Lazarian, "Electric dipole radiation from spinning dust grains," *Astrophysical Journal Letters*, vol. 508, no. 1, pp. 157–179, 1998.

[12] Y. Ali-Haïmoud, C. M. Hirata, and C. Dickinson, "A refined model for spinning dust radiation," *Monthly Notices of the Royal Astronomical Society*, vol. 395, pp. 1055–1078, 2009.

[13] N. Ysard and L. Verstraete, "The long-wavelength emission of interstellar PAHs: characterizing the spinning dust contribution," *Astronomy and Astrophysics*, vol. 509, no. A12, 13 pages, 2010.

[14] Planck Collaboration, "Planck early results 20: new light on anomalous microwave emission from spinning dust grains," *Astronomy & Astrophysics*, vol. 536, no. A20, 17 pages, 2011.

[15] R. Génova-Santos, R. Rebolo, J. A. Rubiño-Martín, C. H.

López-Caraballo, and S. R. Hildebrandt, "Detection of anomalous microwave emission in the pleiades reflection nebula with wilkinson microwave anisotropy probe and the COSMOSOMAS experiment," *Astrophysical Journal Letters*, vol. 743, p. 67, 2011.

[16] M. A. Miville-Deschênes, N. Ysard, A. Lavabre et al., "Separation of anomalous and synchrotron emissions using WMAP polarization data," *Astronomy and Astrophysics*, vol. 490, no. 3, pp. 1093–1102, 2008.

[17] A. Bonaldi, S. Ricciardi, S. Leach, F. Stivoli, C. Baccigalupi, and G. De Zotti, "WMAP 3-yr data with correlated component analysis: anomalous emission and impact of component separation on the CMB power spectrum," *Monthly Notices of the Royal Astronomical Society*, vol. 382, no. 4, pp. 1791–1803, 2007.

[18] T. Ghosh, A. J. Banday, T. Jaffe et al., "Foreground analysis using cros-correlation of external templates on the 7-year Wilkinson Microwave Anisotropy Probe data," *Monthly Notices of the Royal Astronomical Society*, vol. 422, no. 4, pp. 3617–3642, 2012.

[19] S. Ricciardi, A. Bonaldi, P. Natoli et al., "Correlated component analysis for diffuse component separation with error estimation on simulated Planck polarization data," *Monthly Notices of the Royal Astronomical Society*, vol. 406, no. 3, pp. 1644–1658, 2010.

[20] C. G. T. Haslam, C. J. Salter, H. Stoffel, and W. E. Wilson, "A 408 MHz all-sky continuum survey. II—the atlas of contour maps," *Astronomy and Astrophysics*, vol. 47, p. 1, 1982.

[21] C. Dickinson, R. D. Davies, and R. J. Davis, "Towards a free-free template for CMB foregrounds," *Monthly Notices of the Royal Astronomical Society*, vol. 341, no. 2, pp. 369–384, 2003.

[22] A. Bonaldi, L. Bedini, E. Salerno, C. Baccigalupi, and G. De Zotti, "Estimating the spectral indices of correlated astrophysical foregrounds by a second-order statistical approach," *Monthly Notices of the Royal Astronomical Society*, vol. 373, no. 1, pp. 271–279, 2006.

[23] D. P. Finkbeiner, M. Davis, and D. J. Schlegel, "Extrapolation of galactic dust emission at 100 microns to cosmic microwave background radiation frequencies using FIRAS," *Astrophysical Journal Letters*, vol. 524, no. 2, pp. 867–886, 1999.

[24] M. Górski, E. Hivon, A. J. Banday et al., "HEALPix: a framework for high-resolution discretization and fast analysis of data distributed on the sphere," *Astrophysical Journal*, vol. 622, no. 2, pp. 759–771, 2005.

[25] N. Jarosik, C. L. Bennett, J. Dunkley et al., "Seven-year wilkinson microwave anisotropy probe (WMAP) observations: sky maps, systematic errors, and basic results," *Astrophysical Journal*, vol. 192, no. 2, 2011.

[26] D. J. Schlegel, D. P. Finkbeiner, and M. Davis, "Maps of dust infrared emission for use in estimation of reddening and cosmic microwave background radiation foregrounds," *Astrophysical Journal Letters*, vol. 500, no. 2, pp. 525–553, 1998.

[27] D. J. Fixsen, J. L. Weiland, S. Brodd et al., "Comparison of the COBE FIRAS and DIRBE calibrations," *Astrophysical Journal Letters*, vol. 490, no. 2, pp. 482–487, 1997.

[28] K. Silsbee, Y. Ali-Haïmoud, and C. M. Hirata, "Spinning dust emission: the effect of rotation around a non-principal axis," *Monthly Notices of the Royal Astronomical Society*, vol. 411, pp. 2750–2769, 2011.

[29] G. Giardino, A. J. Banday, K. M. Górski, K. Bennett, J. L. Jonas, and J. Tauber, "Towards a model of full-sky galactic synchrotron intensity and linear polarisation: a re-analysis of the Parkes data," *Astronomy and Astrophysics*, vol. 387, no. 1, pp. 82–97, 2002.

[30] F. Boulanger, A. Abergel, J. P. Bernard et al., "The dust/gas correlation at high Galactic latitude," *Astronomy and Astrophysics*, vol. 312, no. 1, pp. 256–262, 1996.

[31] M. A. Miville-Deschênes and G. Lagache, "IRIS: a new generation of IRAS maps," in *Astronomical Society of the Pacific Conference Series*, L. Armus and W. T. Reach, Eds., vol. 357 of *Astronomical Society of the Pacific Conference Series*, p. 167, 2006.